

Article

Color Origin of Red Beds within the Danxia Basin, Southern China

Wang He ¹, Zhijun Yang ^{1,2,*}, Jintao Hu ¹, Ke Zhang ¹ and Hongwei Li ³

- ¹ School of Earth Science and Engineering, Sun Yat-sen University, Zhuhai 519080, China; hewang7@mail2.sysu.edu.cn (W.H.); hujt23@mail2.sysu.edu.cn (J.H.); eeszke@mail.sysu.edu.cn (K.Z.)
- ² Guangdong Provincial Key Laboratory of Geological Processes and Mineral Resources Exploration, Guangzhou 510275, China
- ³ Guangdong Geological Survey Institute, Guangzhou 510080, China; lihongw1981@126.com
- * Correspondence: yangzhj@mail.sysu.edu.cn

Abstract: Sedimentary facies color is an important paleoclimate indicator, but may be unreliable in thick continental red beds. The Danxia Formation is the landscape strata of the Danxia basin, and its color fluctuates between reddish-brown and reddish-purple vertically. This study examined the ferric oxides characteristics, distribution, and mineral composition of the Danxia Formation using a variety of analytical techniques, including optical microscopy, high-resolution scanning electron microscopy, electron probe microanalysis, X-ray diffraction, and micro-Raman spectroscopy. The results indicate that the reddish-brown mineral is composed primarily of fine hematite with traces of goethite, while the reddish-purple mineral consists solely of fine hematite. These hematites exhibit a particle size range of submicron to micron and display various morphologies, including spherical, flake, and fibrous forms. Goethite particles are needle-shaped and often form star-shaped aggregates containing twins. Whole rock geochemical analysis reveals a strong positive correlation between iron and iron group elements, as well as phosphorus and rare earth elements. The findings suggest that the reddening of the Danxia Formation occurs during diagenesis, with fine hematite forming as a result of the alteration of iron-bearing detrital grains. In addition, vertical color variations in Danxia Formation are not attributable to the paleoclimate records, but rather the result of the differentiation of sediment sources. This study provides a novel viewpoint for examining the coloration of thick continental red beds in other regions.



Citation: He, W.; Yang, Z.; Hu, J.; Zhang, K.; Li, H. Color Origin of Red Beds within the Danxia Basin, Southern China. *Minerals* **2023**, *13*, 1054. <https://doi.org/10.3390/min13081054>

Academic Editor: Santanu Banerjee

Received: 22 June 2023

Revised: 5 August 2023

Accepted: 7 August 2023

Published: 9 August 2023



Copyright: © 2023 by the authors. Licensee MDPI, Basel, Switzerland. This article is an open access article distributed under the terms and conditions of the Creative Commons Attribution (CC BY) license (<https://creativecommons.org/licenses/by/4.0/>).

Keywords: continental red beds; Danxia landform; hematite; color heterogeneity

1. Introduction

Danxia landform is a unique type of red-bed landform characterized by its stunning erosion patterns and vibrant colors. These special red-bed landforms have been the subject of study of generations of geomorphologists and geologists [1–5]. In 2010, there are six Danxia landform sites in China recognized as World Natural Heritage sites by UNESCO [6,7]. Despite extensive research, the origin of the captivating colors of the Danxia landform, based on red sandstone and conglomerate, remains unresolved [8]. The primary point of contention among geologists is the source of the fine-grained hematite in the continental red beds responsible for their reddening.

Early geologists held two views on the origin of red beds. One group proposed that red sandstone formed in hot and dry desert environments, with the color derived from fine-grained hematite films coating sand grains [9]. The other group argued that red beds were related to laterite weathering in warm and humid environments, with hematite originating from red clay in the weathering crust [10–13]. Subsequent research revealed that the color of red beds formed during diagenesis and was not dependent on paleoclimatic conditions [14–16]. Currently, most scholars agree that fine-grained hematite originates from the in situ intraformational alteration of iron silicate or oxide detrital particles such as

olivine, pyroxene, hornblende, biotite, ilmenite, and magnetite [17–19]. Others propose that fine-grained hematite results from the diagenetic alteration of iron hydroxide associated with clastic clay grains such as goethite and lepidocrocite [20–23]. This study examines the distribution, mineralogy, and morphology of hematite from the Danxia formation, explores the origin and formation process of fine-grained hematite, and discusses the color variations of Danxia formation and implications for other continental red beds.

2. Geological Setting

The study area is situated in the graben basin of northern Guangdong province in China, where nearly 4000 m of thick Cretaceous continental red beds have developed (Figure 1) [24,25]. These red beds are represented by the Changba and Danxia Formations, with the Danxia Formation being the primary scenic rock of the Danxia landform (Figure 1a) [2,26]. This formation has a thickness of approximately 1000 m and contains three members from bottom to top: Bazhai, Jinshiyan, and Baizhaiding [24,27] (Figure 2). The Bazhai Member is primarily composed of thick fine- to coarse-grained sandstone and conglomerate that are mostly maroon and reddish-purple in color. The particle size ranges from 2 to 10 mm, with poor roundness and sorting [28]. The Jinshiyan Member consists of fine feldspathic quartz sandstone with large eolian cross-bedding and is reddish-brown and maroon in color. In some parts, there are lenticular gravelly sandstones, while the upper part contains medium-thin mudstone, silty mudstone, and calcareous layers [28]. The Baizhaiding Member is made up of maroon conglomerate and pebbly sandstone, partially intercalated with reddish-purple thin silty mudstone. The gravel is primarily composed of quartz sandstone, vein quartz, and limestone, with minor traces of granite and flint. The Bazhai and Baizhaiding Members are dominated by alluvial fan facies, while the Jinshiyan Member is characterized by dry valley, desert, and salt-lake facies [29]. The base of the Danxia Formation is marked by a thick layer of conglomerates that are in conformable contact with the underlying Changba Formation [26,30] (Figure 2). This formation consists of reddish-purple clastic units evolved from fluvial and lacustrine environment [28].

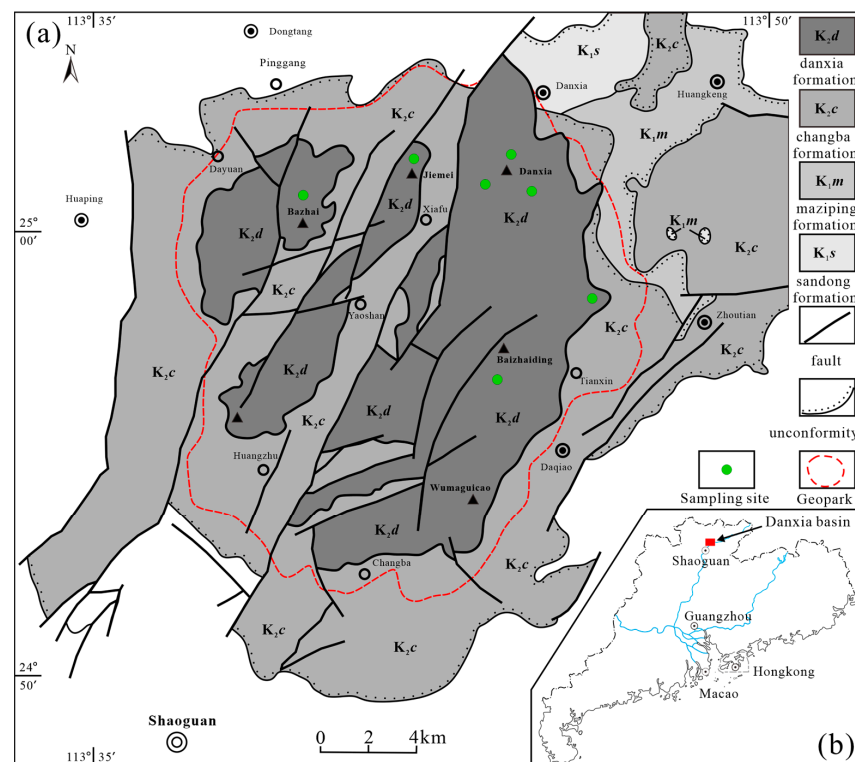


Figure 1. (a) Simplified geological map of Danxia basin (modified from reference [30]). (b) The location of Danxia basin in northern Guangdong province, China.

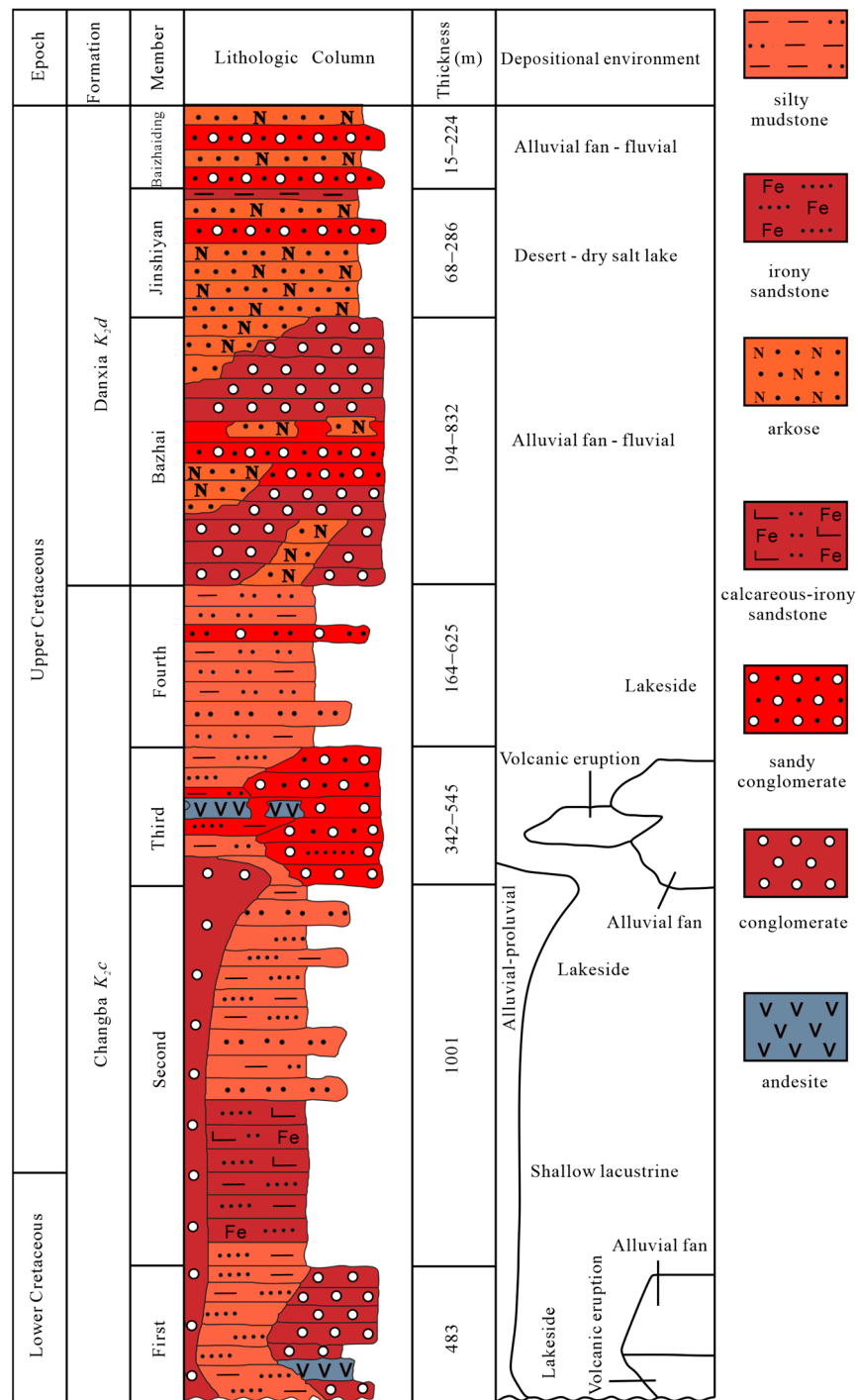


Figure 2. Generalized stratigraphical column of the Danxia basin (modified from reference [28]).

3. Materials and Methods

All samples of forty red facies and two bleaching facies covering various colors were collected by portable drilling rig from seven localities in the Danxia basin. The representative rock cutting sections were initially observed with Ultra-Depth Three-Dimensional Microscope (UDTDM) (VHX-5000, KEYENCE, Osaka, Japan) for ferric oxides on the surface of detrital grains. Polished thin sections of all samples were examined with optical microscopy using transmitted, reflected, and incident light. Incident light imaging was carried out by illuminating the sample with an external light source at an angle of approximately 45 degrees to identify fine-grained ferric oxide particles [31].

Selected polished thin sections were carbon coated and examined for mineralogical and textural characterization of altered iron-bearing grains and authigenic hematite in backscattered electron mode (BSE) in a Quanta 400 field emission scanning electron microscope (FESEM) (FEI, Hillsboro, OR, USA) equipped with an OXFORD INCS350 energy dispersive X-ray spectroscopy detector (EDX, Oxford Instruments, Oxford, UK). The morphology of ferric oxides around detrital grains and filling in pore spaces were observed by an Ultra-high Resolution Scanning Electron Microscope (Regulus 8230, Hitachi, Japan) equipped with flat insertion energy spectrum and YAG backscattered electron detector with a spatial resolution of 10 nm.

Mineralogical characteristics of the bulk samples were determined by X-ray powder diffraction (XRD, Empyrean, Malvern Panalytical, Almelo, The Netherlands) analyses, which were carried out with an Empyrean diffractometer using $\text{CuK}\alpha$ radiation, operated at 30 kV and 20 mA and speed of $2.4^\circ 2\theta/\text{min}$, at the Instrumental Analysis and Research Center, Sun Yat-Sen University, China. Micro-Raman spectra were recorded using an inVia Qontor (Renishaw, Gloucestershire, UK) Raman microscope equipped with a 785 nm laser. The beam with a diameter of $1\ \mu\text{m}$ was focused through a $50\times$ objective with a power of 335 mW. Each spectrum was captured for 10 s and averaged by 5 successive scans with a resolution of $1\ \text{cm}^{-1}$.

Whole-rock geochemical analyses of major and trace elements were performed on sixteen selected samples at Guangzhou Tuoyan Analytical Technology Co., Ltd., Guangzhou, China. Major elements were analyzed using a Rigaku Primus II X-ray fluorescence spectrometer (XRF), while trace elements, including rare earth elements, and their concentrations were measured by inductively coupled plasma mass spectrometry (Thermo Scientific iCAP RQ ICP-MS). During the test, GSR-3, GSD-4, GSD-6, OU-6, GSR-12, GSR-13, NOD-P-1, OU-6, BCR-1, and GBPG-1 were used as standard samples to monitor the accuracy of the test results. The relative standard deviation (RSD) of the test results was better than 5%.

4. Results

4.1. Coloring Properties

The color of the Danxia Formation is not uniform; instead, it fluctuates vertically, transitioning to shades of brown and purple. This results in a spectrum of reddish shades, including reddish-brown, maroon, and reddish-purple (Figure 3). Additionally, Danxia Formation also exhibits variations in lightness and darkness within the same hue. Samples with the most distinct color differences, such as reddish-brown and reddish-purple, were selected for comparison (Figure 4). It is difficult to distinguish the coloring minerals under plane polarized light (Figure 4c,g). However, under incident light, it becomes clear that there are two main types of coloring minerals—red and yellow—coexisting in the reddish-brown sample (Figure 4f,h), while the reddish-purple sample contains mostly red minerals (Figure 4b,d). These discoveries indicate that the color variations exhibited by Danxia formation might be controlled by content and mineralogy of coloring minerals. And the presence of other minerals within the rock adds further subtlety to the color variations (Figure 4f).

4.2. Distribution

In the Danxia Formation, red minerals that contribute to the overall color of the rocks primarily exist in two states: dispersed and granular (Figures 5 and 6). Despite the lower concentration, dispersed coloring minerals are responsible for the overall bright red color of the red beds. These minerals are generally distributed on the surface of detrital grains or along overgrowth edges and can be observed almost everywhere (Figure 5a–c). Dispersed coloring minerals can also be found in the matrix or fractures between detrital grains, as shown in Figure 5d–f. The distribution of dispersed coloring minerals is not uniform and often occurs in localized areas of enrichment.



Figure 3. Core specimens of red beds with gradual fluctuations in color between reddish-brown and reddish-purple from Danxia formation.

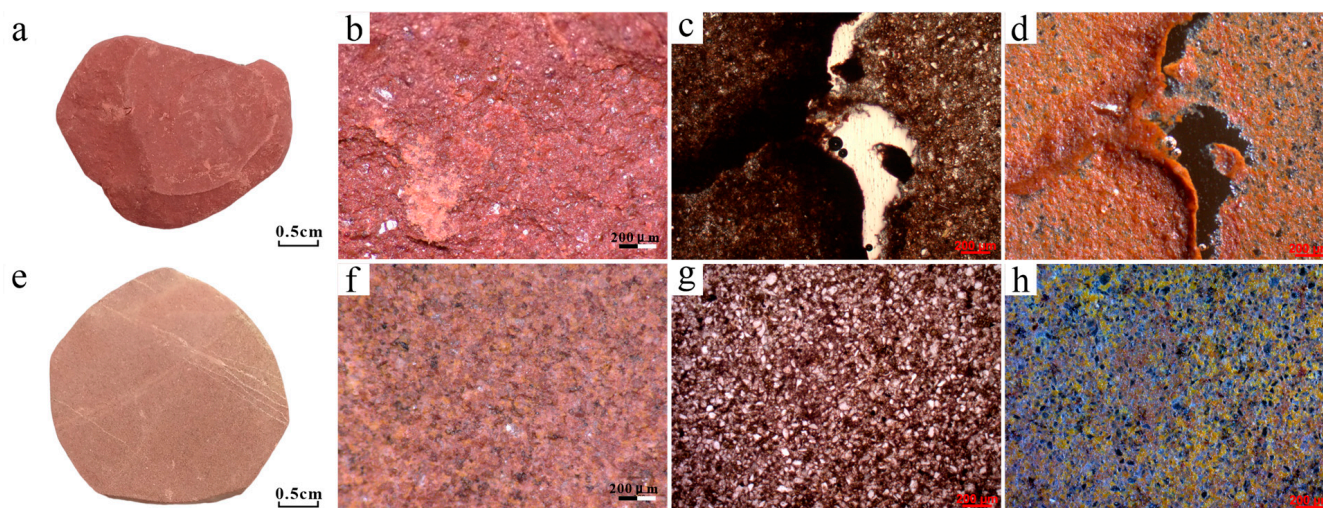


Figure 4. The differences between reddish-purple mudstone and reddish-brown siltstone observed through various detection methods. (a) Hand specimen of reddish-purple mudstone. (b) Image of (a) captured with Ultra-Depth Three-Dimensional Microscope (UDTDM). (c) Plane polarized light (PPL) micrograph of (a). (d) Incident light (IL) micrograph of (c). (e) Hand specimen of reddish-brown siltstone. (f) Image of (e) captured with UDTDM. (g) PPL micrograph of (e). (h) IL micrograph of (g).

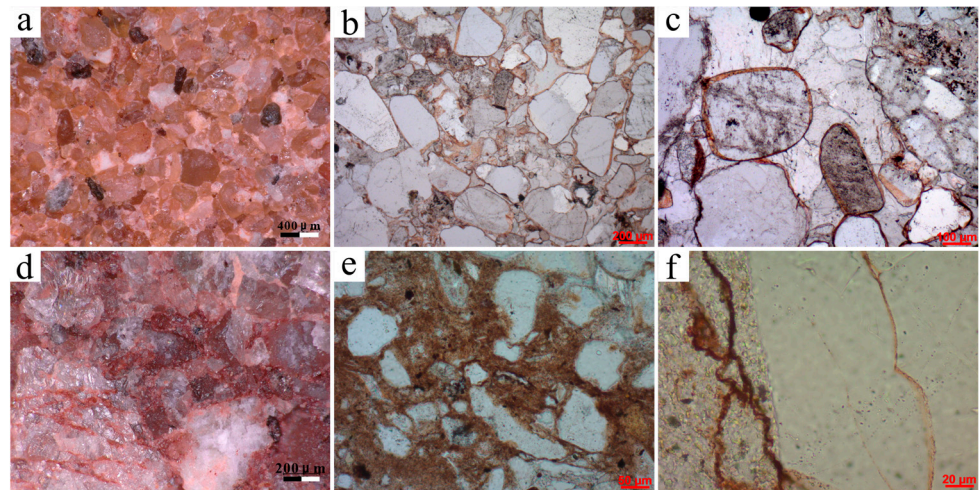


Figure 5. (a) Dispersed coloring minerals coating on the surface of detrital grains, reddish-brown sandstone, UDTDM. (b) Dispersed coloring minerals enclosed by carbonate cement, PPL micrograph of (a). (c) Partially enlarged view of (b). (d) Dispersed coloring minerals disseminated into the matrix and fractures, Reddish-purple conglomerate, UDTDM. (e) Dispersed coloring minerals in the matrix, PPL. (f) Dispersed coloring minerals in the fractures, PPL.

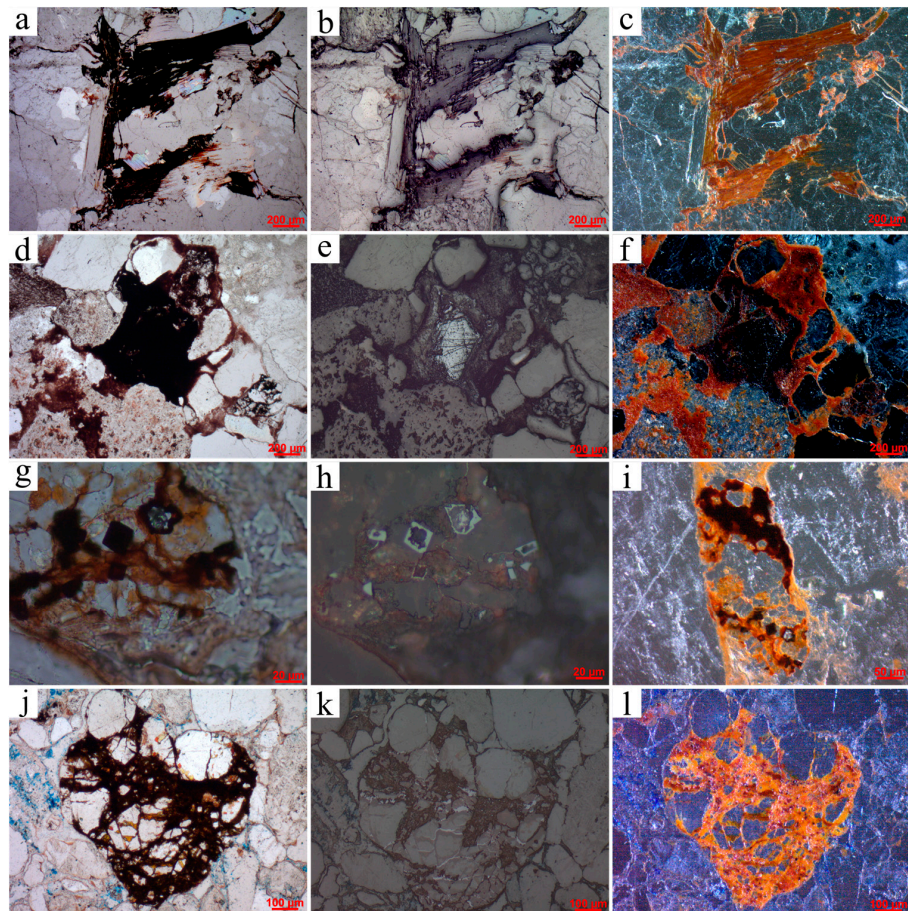


Figure 6. (a) Distorted, squeezed, and altered biotite remains, PPL. (b) Reflected light (RL) view of (a). (c) IL view of (a). (d) Altered ilmenite progressing from the margin of the grain inward, PPL. (e) RL view of (d). (f) IL view of (d). (g) Altered magnetite particles preferentially destroyed from the grain interior, PPL. (h) RL view of (g). (i) IL minified view of (g). (j) Clastic grains cemented by rich hematite, PPL. (k) RL view of (j). (l) IL view of (j).

Granular coloring minerals are formed by the alteration of iron-bearing detrital minerals such as biotite, ilmenite, and magnetite, and typically occur around these mineral grains or within fracture cracks (Figure 6). Under reflected light, general granular coloring minerals appear black while enriched granular coloring minerals appear bright white (Figure 6b,e,h,k). Under incident light, general granular coloring minerals take on a bright red hue while enriched granular coloring minerals appear black (Figure 6c,f,i,l). However, when viewed under plane polarized light, almost all granular coloring minerals appear dark red or even black (Figure 6a,d,g,j). Due to their heavy concentration, granular coloring minerals have a limited impact on the overall color of the Danxia Formation. And these appear to be an important source or precursor of dispersed coloring minerals.

4.3. Geochemistry

The results of the geochemical analysis of the reddish and bleached samples are summarized in Table 1 and Tables S1 and S2 (Supplementary Materials). The samples are characterized by high SiO₂ (55.08–84.91 wt.%) moderate Al₂O₃ (5.50–16.81 wt.%), and low K₂O (1.50–4.40 wt.%) and MgO (0.48–1.27 wt.%) contents. CaO (1.5–20.2 wt.%) and LOI (19.3–25.4 wt.%) show a strong positive correlation, mainly due to the calcite content in the samples from calcareous cement (Figure 7a). In addition, CaO also exhibits a strong negative correlation with SiO₂ (Figure 7b).

Table 1. Major elements composition from bulk samples of fluctuant colors.

Sample	Color	SiO ₂ wt.%	TiO ₂ wt.%	Al ₂ O ₃ wt.%	TFe ₂ O ₃ wt.%	MnO wt.%	MgO wt.%	CaO wt.%	Na ₂ O wt.%	K ₂ O wt.%	P ₂ O ₅ wt.%	LOI wt.%	SUM wt.%
H-1	reddish-brown	55.45	0.44	9.23	3.85	0.07	0.52	13.71	0.09	1.50	0.16	14.30	99.30
H-2	reddish-brown	78.61	0.16	7.58	0.90	0.01	0.61	3.07	0.68	2.28	0.03	4.27	98.19
H-3	reddish-purple	61.77	0.17	10.33	1.62	0.02	1.27	9.19	0.64	3.71	0.03	10.15	98.89
H-4	darkreddish-brown	83.32	0.17	7.81	1.00	0.02	0.88	0.22	0.28	2.77	0.04	2.35	98.85
H-5	lightreddish-brown	84.91	0.14	7.34	0.72	0.00	0.59	0.16	0.15	2.08	0.01	2.12	98.22
H-6	reddish-brown	83.05	0.15	8.18	0.94	0.03	0.70	0.19	0.14	3.49	0.03	1.96	98.86
H-7	reddish-purple	70.91	0.20	7.52	1.34	0.02	0.84	7.53	0.36	2.96	0.02	7.68	99.36
H-8	reddish-purple	66.52	0.17	9.21	1.17	0.02	0.79	7.78	0.53	4.40	0.04	8.29	98.92
H-9	reddish-brown	74.89	0.18	6.33	0.92	0.01	0.76	6.43	0.48	2.19	0.02	6.62	98.82
H-10	reddish-purple	59.18	0.30	7.46	1.92	0.03	0.88	14.05	0.12	2.28	0.05	13.13	99.40
H-11	reddish-purple	74.70	0.20	7.47	1.82	0.01	0.76	5.57	0.10	2.48	0.08	6.15	99.35
H-12	maroon	72.36	0.13	6.45	0.96	0.02	0.48	8.20	0.10	2.56	0.04	7.84	99.13
H-13	maroon	70.27	0.16	7.92	1.25	0.05	1.18	7.27	0.12	2.99	0.04	7.83	99.07
H-14	reddish-purple	59.88	0.18	7.11	1.08	0.04	0.85	13.77	0.12	2.71	0.03	12.68	98.44
B-1	pale	77.03	0.16	7.11	0.45	0.01	0.49	4.56	0.71	2.68	0.02	5.29	98.50
B-2	light-green	55.08	0.09	5.50	0.36	0.02	0.60	18.23	0.12	2.70	0.02	15.64	98.36
	average	69.95	0.22	8.20	1.27	0.03	0.78	7.37	0.46	2.73	0.06	—	—
	abundance of sandstones in Eastern China [32]	72.63	0.49	10.91	3.55	0.06	1.26	2.52	1.41	2.40	0.09	—	—

Note: '—' means null value; LOI: Loss on ignition.

The most remarkable difference in all elements is the total amount of iron, given as TFe₂O₃, which is depleted compared to sandstones in the eastern part of China by up to 64% (Table 1). And even then, TFe₂O₃ exhibits a strong positive correlation with the red minerals (Figure S1, Supplementary Materials), which is typical of red beds. Moreover, the content of TFe₂O₃ is much lower in the bleached samples because of the absence of iron-bearing grain coatings (Table 1). Despite this, interestingly, TFe₂O₃ shows a significant positive correlation with TiO₂, P₂O₅, Sc, Cr, Co, Ni, Cu, Zn, and REE (Rare Earth Elements) in all rock types, and are somewhat color-dependent, in that purplish red beds have highest

concentrations, brownish and maroon red rocks have moderate, and bleached samples lowest (Figures 7f and 8). In addition, $TfFe_2O_3$ also shows a moderate positive correlation with Al_2O_3 and MnO (Figure 7d,e), but displays a moderate negative correlation with SiO_2 (Figure 7c). However, these elements do not appear to vary significantly with color variations of red beds.

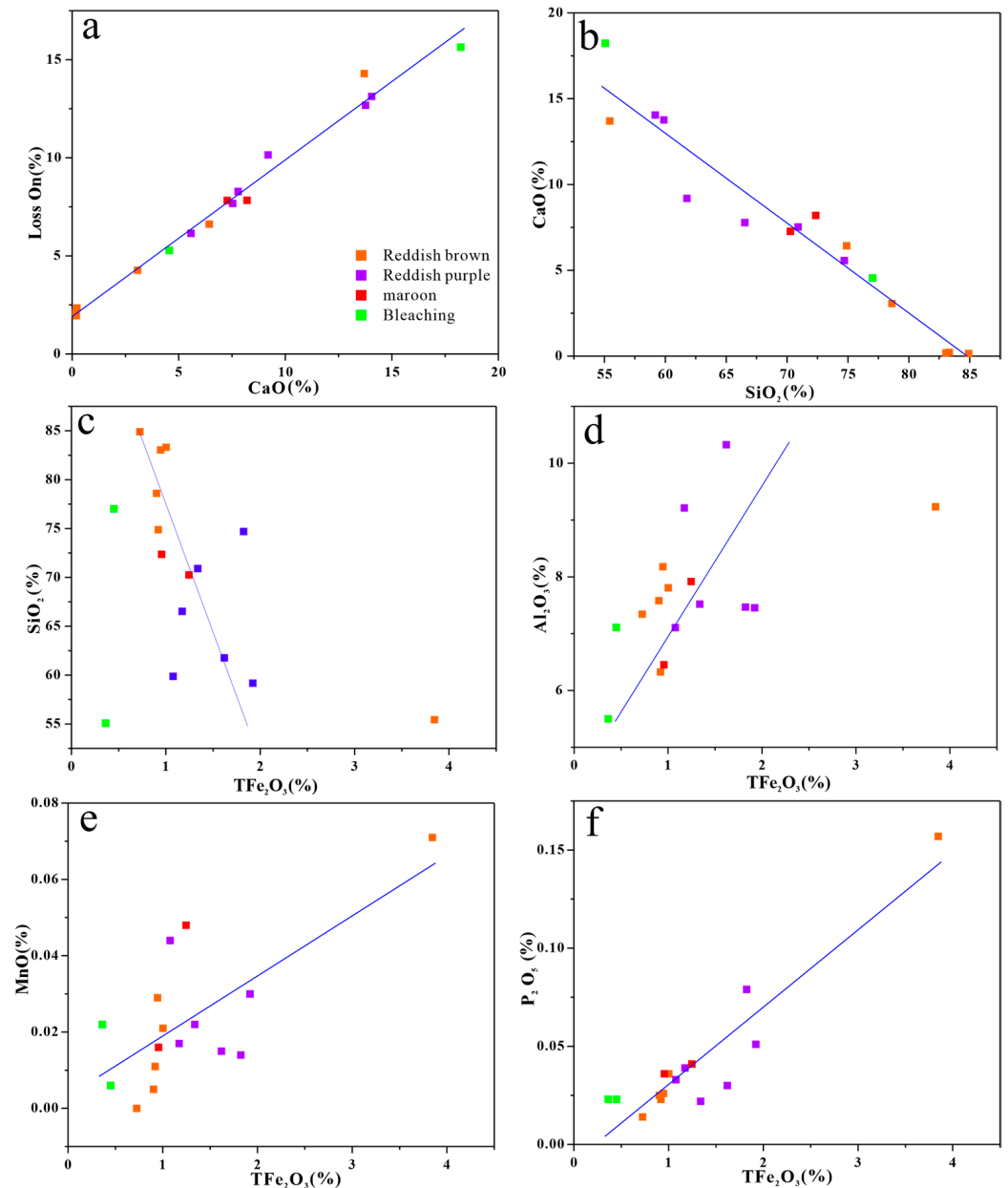


Figure 7. Binary plots of selected major elements: (a,b) CaO vs. Loss On and SiO_2 ; (c–f) $TfFe_2O_3$ vs. SiO_2 , Al_2O_3 , MnO , and P_2O_5 , respectively.

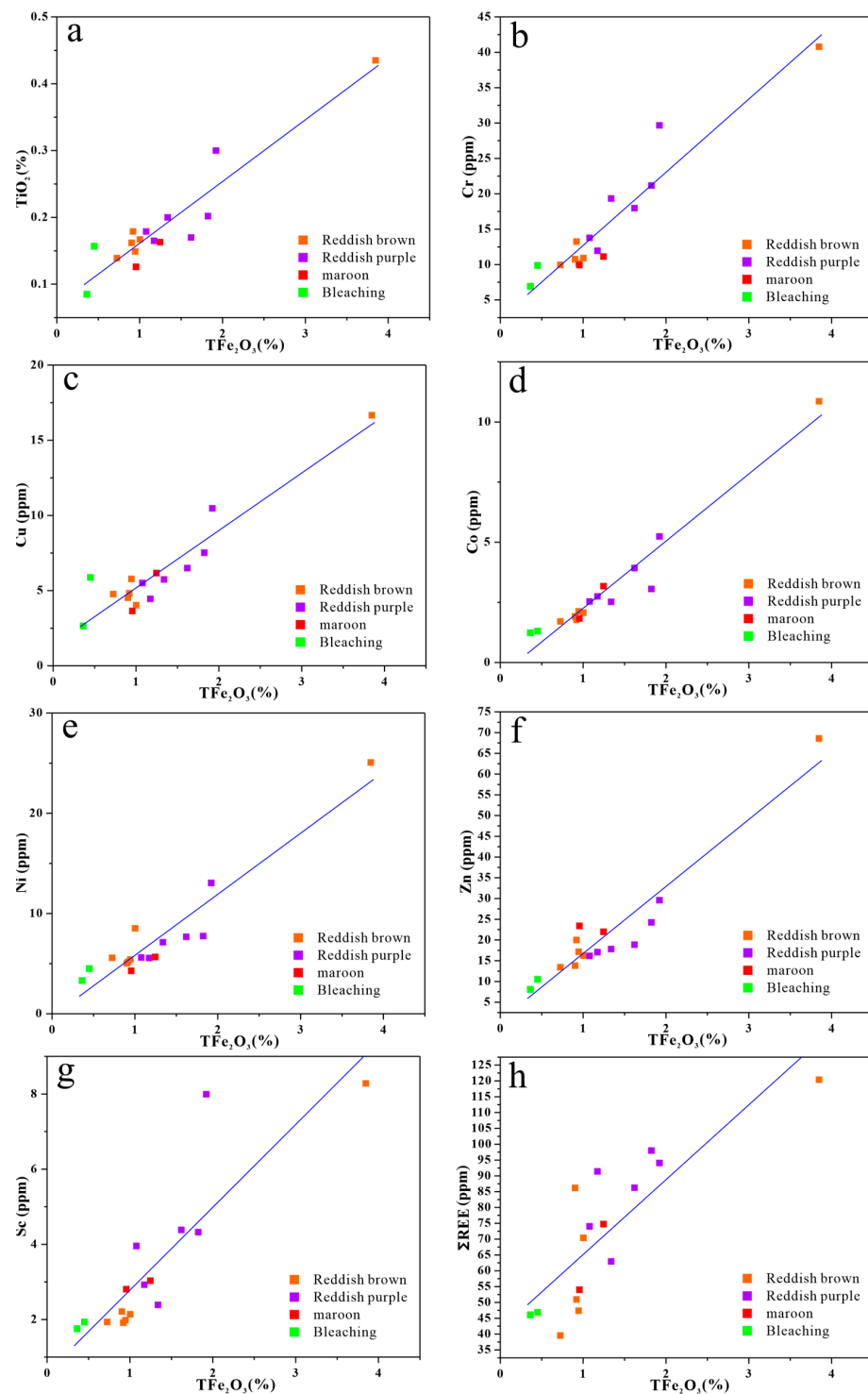


Figure 8. Binary plots of selected trace elements: (a–h) TFe_2O_3 vs. TiO_2 , Cr, Cu, Co, Ni, Zn, Sc, and ΣREE , respectively.

4.4. Mineralogy

X-ray diffraction (XRD) analysis of representative red bed samples reveals that quartz (α - SiO_2) is the predominant mineral, with its three strongest peaks at 4.26 Å, 3.34 Å, and 1.82 Å, corresponding to the (100), (101), and (2–12) planes (PDF#97-003-9830), respectively (Figure 9a). Owing to relatively low concentrations, however, the most concerned hematite (α - Fe_2O_3) is characterized by four weak intrinsic peaks at 2.70 Å, 2.52 Å, 2.20 Å, and 1.69 Å, corresponding to (104), (110), (113), and (116) lattice planes (PDF#01-089-0599), respectively

(Figure 9a). Figure 9b displays the micro-Raman spectra of hematite and quartz in the selected sample alongside the standard pattern from the RRUFF database (Raman spectra, X-ray diffraction and chemistry data for minerals). As the testing points vary from ① to ⑤, the concentration of red minerals decreases, leading to weaker Raman characteristic peaks of hematite and stronger peaks of quartz. This contrast in Raman peaks highlights the positive correlation between hematite and red minerals in the Danxia formation.

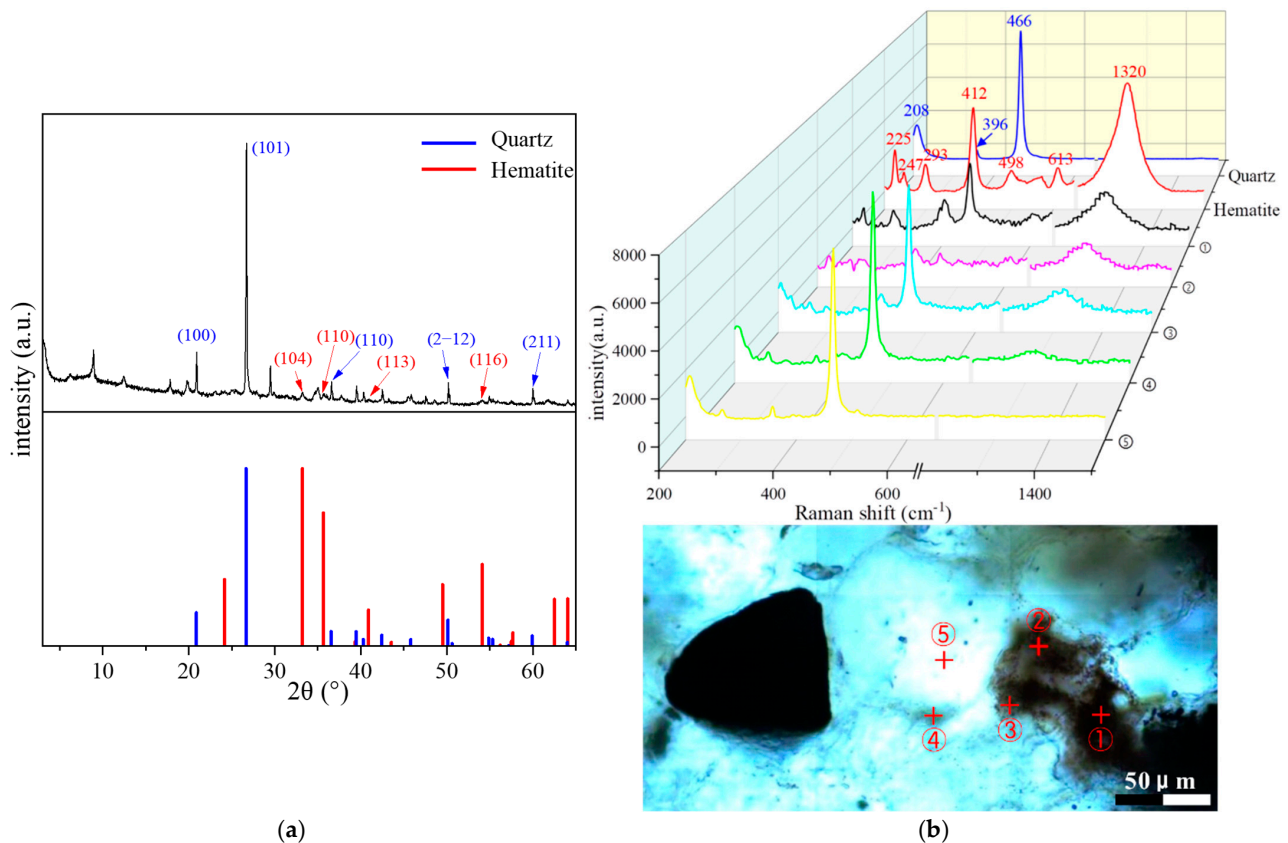


Figure 9. (a) XRD pattern of the reddish-brown sandstone as well as the standard quartz and hematite as reference; (b) The micro-Raman spectra of the reddish-brown sandstone, along with standard quartz and hematite as references. The concentration of hematite decreases as the testing points vary from ① to ⑤.

4.5. Micromorphology

SEM images of strongly altered iron-containing mineral indicate the spatial and temporal inheritance correlation between authigenic fine hematite crystals and unstable iron-bearing grains (Figures 10–12). Hematite in the Danxia formation commonly occurs as enriched and well-crystalline around the altered iron-bearing grains, while being relatively depleted and finer-grained away from these grains. For instance, ilmenite grains have been highly altered along their edges and are mostly replaced by hematite and anatase (Figure 10a–c). Much of the hematite occurs as euhedral clusters of microcrystals growing in fissure spaces near the altered ilmenite (Figure 10d,e), with the remainder of the mineral occurring as finely dispersed grains in the matrix (Figure 10f). Micas (mostly biotite) that have been intensively deformed and altered during diagenetic processes are commonly replaced by lenticular or lath-shaped hematite along their cleavage planes (Figure 11). Meanwhile, hematite also occurs as spherical aggregates within abundant spaces which were supported by the biotite fragments (Figure 11b,c) and as fibrous aggregates infilling in insufficient and smaller voids (Figure 11f). In some instances, hematite occurs as replacement of magnetite altered along the internal grains (Figure 12a–c).

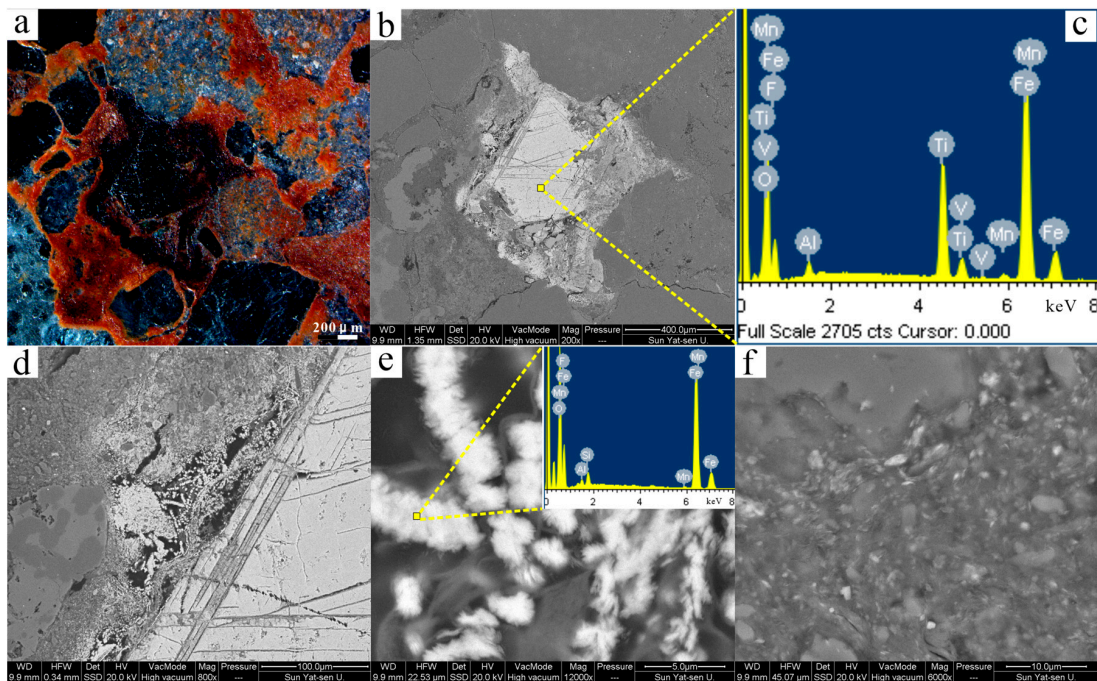


Figure 10. (a) Incident light (IL) image showing fine-grained hematite surrounding altered ilmenite in reddish-purple sandstone. (b) BSE image of (a) captured using SEM. (c) Energy-dispersive X-ray spectroscopy (EDX) pattern of the ilmenite. (d) Enlarged view of (b) highlighting the boundary of the ilmenite and the fine-grained hematite. (e) Larger view of (d) providing more details of euhedral bead-like hematite aggregates, with an inset showing the corresponding EDX pattern. (f) Enlarged view of a section of (d) displaying microfine hematite mixed with clay minerals.

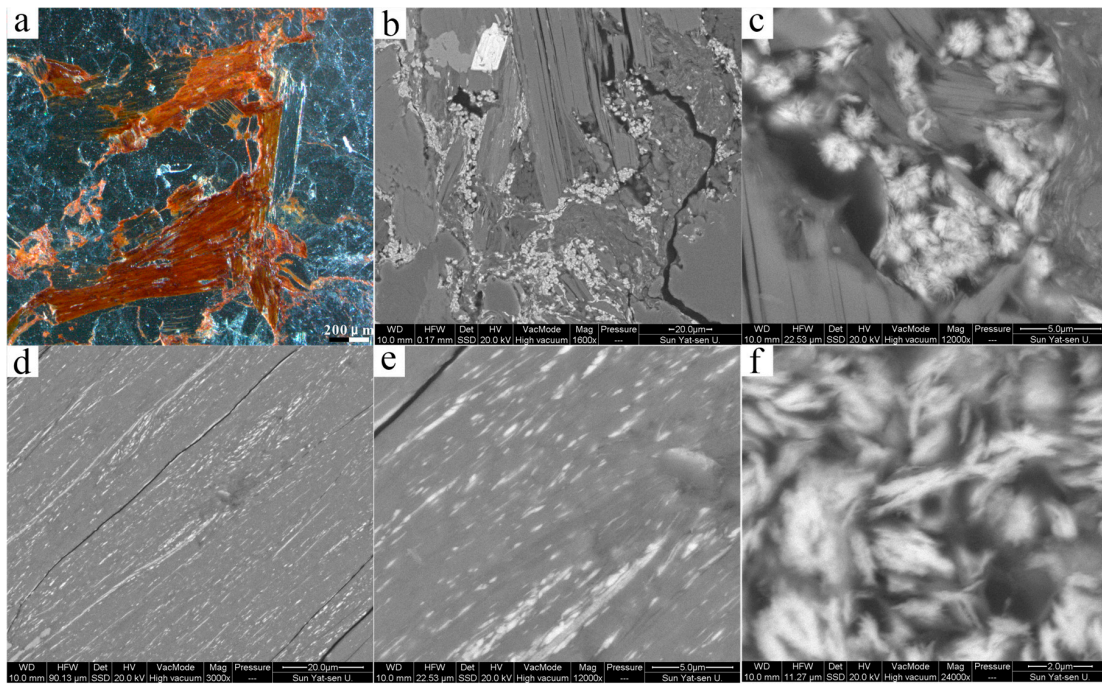


Figure 11. (a) Incident light (IL) image showing fine-grained hematite filling in altered biotite in reddish-purple sandstone. (b) Section of BSE image of (a) captured using SEM. (c) Enlarged view of (b) showing the euhedral spherical hematite aggregates enclosed by the biotite fragments. (d) Fine-grained hematite laths aligned in cleavage of biotite. (e) Larger view of (d) providing more details of hematite recrystallization in situ. (f) Fibrous hematite aggregates.

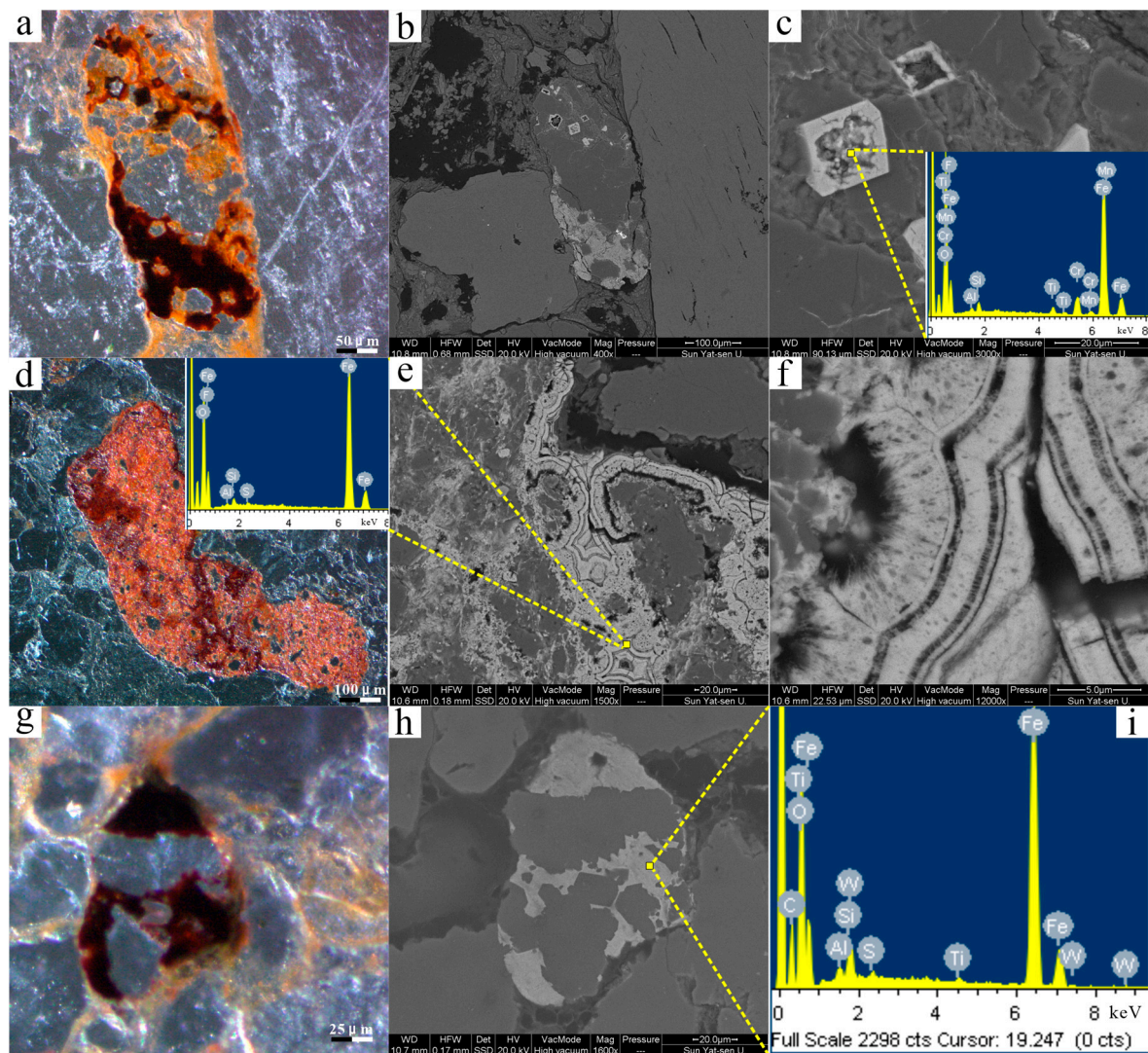


Figure 12. (a) Incident light (IL) image showing euhedral detrital ferric oxide (presumably magnetite) altered along inside the mineral grains and recrystallized in situ or around. (b) BSE image of (a) captured using SEM. (c) Enlarged view of (b) showing the residue of precursors and the authigenic globular fine-grained hematite, with an inset showing the corresponding EDX pattern. (d) IL image showing hematite precipitated around detrital grains. (e) BSE image of (a) captured using SEM, with an inset showing the corresponding EDX pattern. (f) Larger view of (e) providing more details of hematite shaped in a ring structure containing authigenic fibrous hematite on the surface. (g) IL image showing quartz grains cemented by recrystallized hematite. (h) BSE image of (a) captured using SEM. (i) EDX pattern of the hematite in (h).

In many cases, iron-bearing minerals have completely been replaced by hematite occurring as isolated large polycrystals without any remaining residuals (Figure 12d–i). These hematite grains also commonly cement and encase the adjacent detrital (Figure 12b,e,h). In addition, the alteration products usually penetrate the fracture channels and recrystallize as euhedral hematite and goethite aggregates (Figure S2, Supplementary Materials).

High-resolution SEM images of iron-containing coatings show microfine ferric oxides/oxyhydroxides disseminated on the detrital grains (quartz and feldspar), and mixed with clay minerals (illite and smectite) in the matrix (Figure 13). Thin coatings are sometimes developed at grain contacts and covered by thin quartz overgrowths or calcite cement preserving reddish rims (Figures 13 and S3). The coatings consist essentially of microfine hematite and goethite. Goethite appears as star-shaped clusters containing twins in sub-

micron to nanoscale sizes filling in pore spaces and clay mineral wafers (Figure 13a,b). Goethite could be observed in reddish-purple samples, but with an abundance clearly less than that in reddish-brown samples. Much of the hematite occurs as spherical microcrystals distributed among clay minerals, with the remainder of ultrafine crystals growing on the detrital grains (Figure 13d–f). Unlike goethite, hematite is abundant both in reddish-brown and reddish-purple samples.

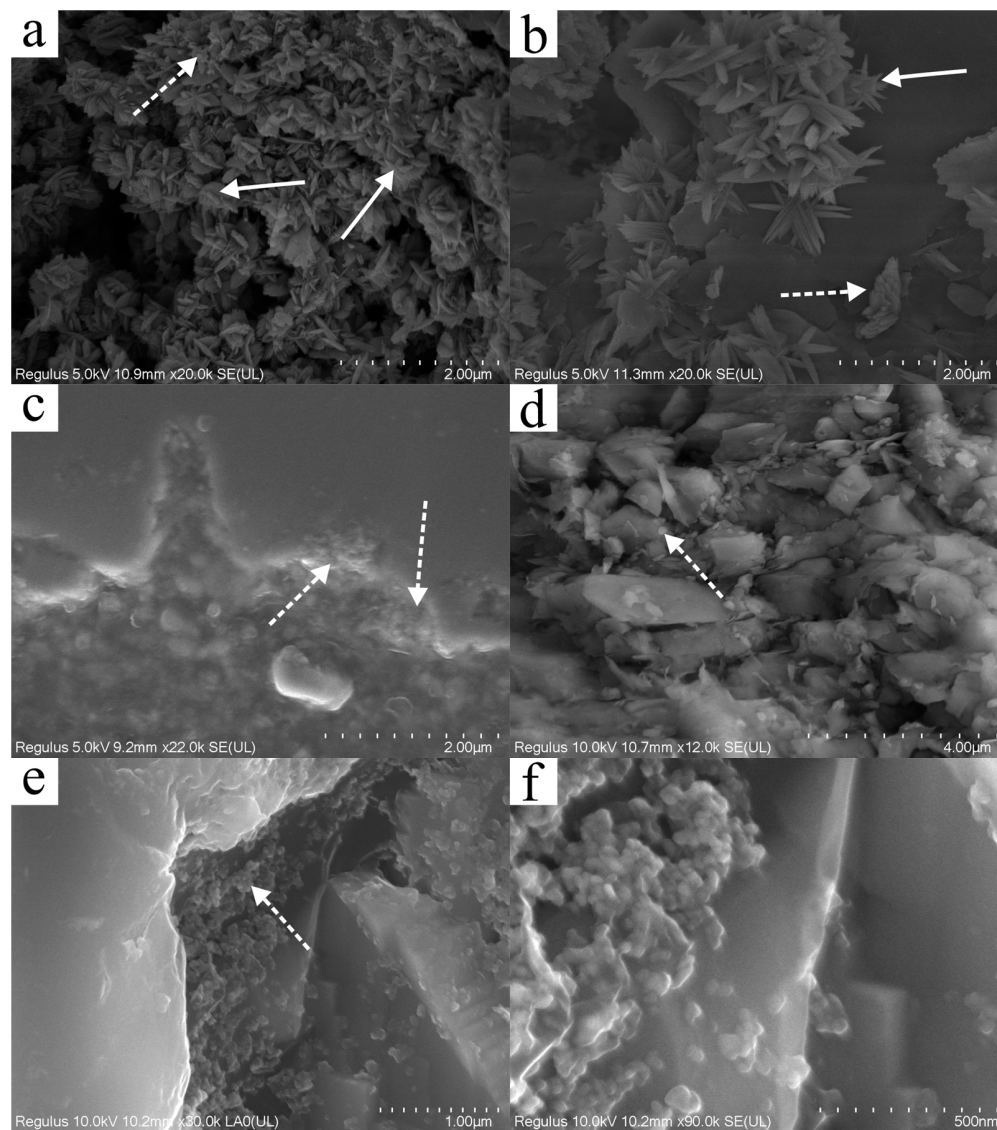


Figure 13. High-resolution SEM images of microfine ferric oxides (submicron to nanoscale) in red beds from Danxia Mountain. (a) Star-shaped goethite clusters (white arrows) speckled with few hematite particles (dashed white arrow). (b) Star-shaped goethite (containing twins) and rosette hematite (dashed white arrow) developed on the surface of clay minerals. (c) Microfine hematite particles (dashed white arrow) filled into the bay-shaped edges of quartz grain. (d) Fine and dispersed hematite (dashed white arrow) distributed among clay minerals. (e) Spherical (or round-shaped) nanoscale hematite particles (dashed white arrow) attached on the detrital quartz. (f) Larger view of (e).

5. Discussion

5.1. The Role of Hematite and Goethite

Given the above, the captivating color of red beds is due to the presence of microfine hematite, as reported in previous studies [18,33,34]. In addition, this study has also identi-

fied the role of goethite in the coloration of the Danxia Formation. Although less prevalent than hematite, the presence of goethite imparts a subtle brown hue to the sediments. The reddish-purple in red beds may be determined by the content, arrangement, and particle size of hematite [8,35–37]. While cation substitution can slightly adjust the color of hematite [38], it does not appear to have a decisive impact on the overall coloration of the red beds. Instead, variations in the relative content and particle size of hematite and goethite principally account for the observed color differences between reddish-brown and reddish-purple in the Danxia formation.

5.2. Iron Sources of Fine-Grained Hematite

As noted in the introduction, geologists agree that diagenesis produces fine hematite, but its source remains a topic of debate. These disputes indicate that the hematite in red beds may have various sources. However, it is hypothesized that fine-grained hematite in most red beds are derived from both iron-bearing grains (hornblende, biotite, ilmenite, etc.) and iron hydroxides associated with clays. Different red beds may contain varying proportions of these minerals [20].

Whole-rock geochemical analysis has revealed a strong positive correlation between iron, titanium, and other iron group elements in the Danxia Formation (Figures 7 and 8). These elements may have been released during the alteration of iron-bearing minerals and not transported over long distances. Three reasons support this argument. Firstly, iron not only exhibits a high correlation with iron group elements but also has a strong association with phosphorus (Figure 7f). In sediments, ferric oxides or hydroxide phases are typically linked with active phosphorus, forming what is known as iron-bound phosphorus (Fe-P) [39–41]. Secondly, as the color deepens, the contents of iron group elements increase in tandem, suggesting a relationship with color-causing active ferric oxides (Figure 8). Finally, microscopic observations of the Danxia Formation revealed a scarcity of metastable iron-magnesium minerals such as olivine and pyroxene [16]. Most iron-bearing minerals in sediments are relatively stable in the depositional environment such as biotite, ilmenite, and magnetite [42,43]. However, even these minerals are undergoing alteration or have been completely altered. As a result, it can be inferred that the Danxia Formation represents the end member dominated by altered iron-bearing particles, with a relatively scarce clay source. Fine-grained hematite predominantly originates from the recrystallization of iron magnesium silicate or ferric oxide particles following the diagenetic process.

5.3. Diagenetic Reddening

During the Late Cretaceous period, tectonic activities caused the intermountain basins near Danxia and Nanxiong in South China to continue to subside [44–46]. In this process, the Danxia Basin continued to receive detrital sediments from surrounding areas [47,48]. The color of these detrital sediments generally originated from a small amount of iron hydroxide associated with clay, resulting in early sediment colors ranging from yellow to light brown [15] (Figure 14). During the period from syndeposition to diagenesis, iron-bearing mineral particles such as iron magnesium silicate formed under high temperature and/or high pressure began to undergo alteration (Figure 14). The intrusion of oxygen-containing interstitial water and brine caused relatively unstable minerals such as olivine and pyroxene to quickly alter and disappear in red beds, leaving few traces [43]. In contrast, the alteration process of relatively stable minerals such as biotite and ilmenite are more prolonged, making them the primary heavy minerals present in the Danxia Formation. Alteration often occurs selectively based on the crystal structure of the mineral grain itself and can be mainly classified into two types: alteration progressing from the edge of the grain inward and alteration along the internal cleavage plane of the grain [49] (Figures 10–12). As alteration products, fine hematite initially emerges around iron-bearing mineral particles or distributes along mineral cleavage pores before gradually diffusing to more distant locations with pore water. Eventually, some of the hematite is distributed in the matrix and fractures of the red bed in the form of clusters and disseminations, while another portion

mixes with clay minerals and surrounds the surface of clastic minerals to form coatings. Part of these coatings are enveloped by overgrowths and carbonate cements in later stages (Figure 14). In this way, these finely grained hematites, with their uniform distribution but low content, become the primary force responsible for the bright red appearance of the Danxia formation.

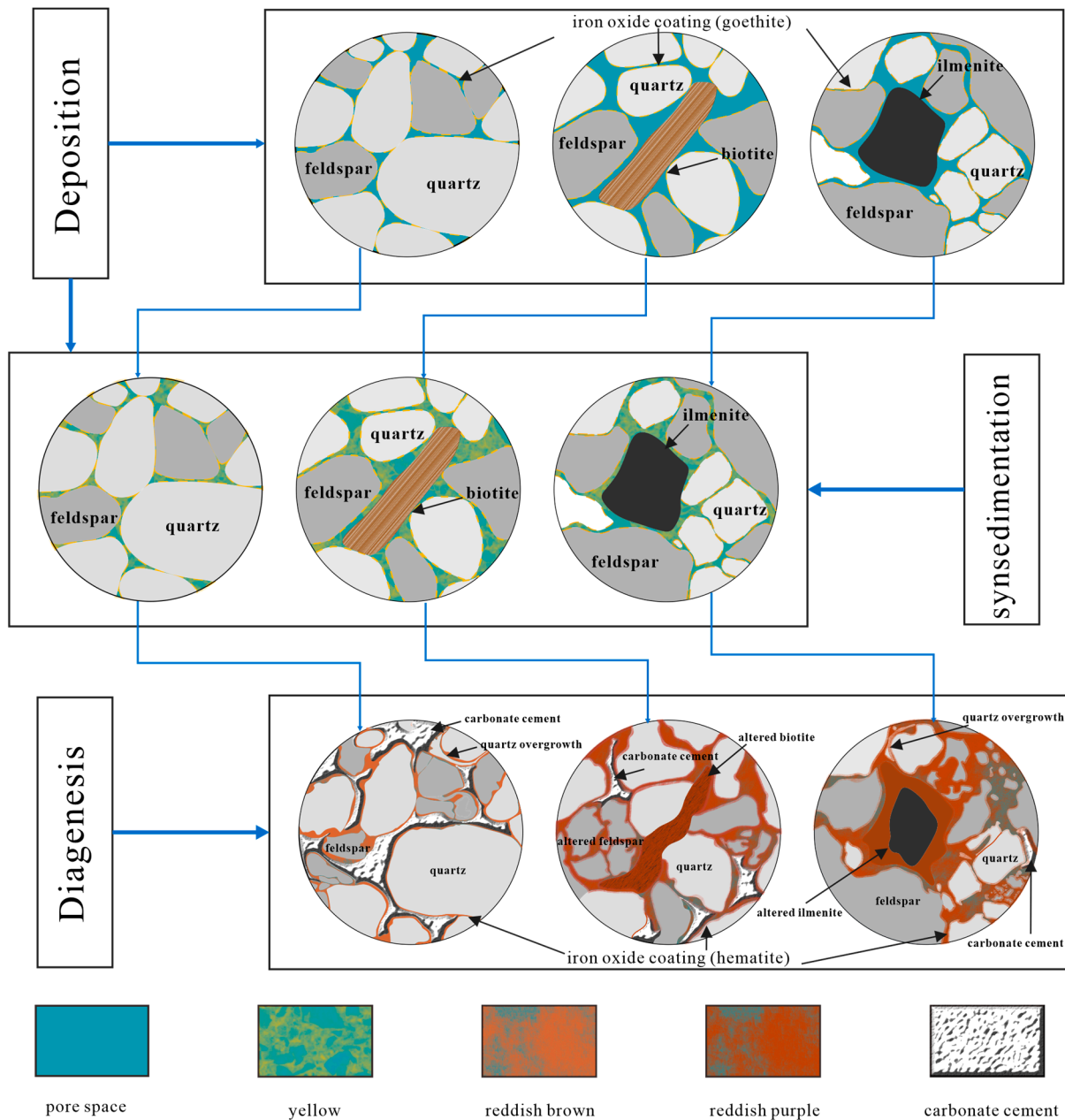


Figure 14. Synoptic sketch of microscopically identified features during reddening of Danxia formation. During the early stage of sedimentation, sediments are primarily deposited mechanically, with traces of ferric oxides adhering to the surface of detrital grains, resulting in a light-yellow color. As sedimentation progressed, chemical deposition became the dominant process, with ferric oxides infiltrating the gaps between detrital grains through true solutions, colloids, or clay. This resulted in a yellow or brown color. During diagenesis, iron-bearing minerals undergo alteration, releasing iron into the interstitial materials in the form of fine hematite. This process is accompanied by feldspar dissolution, quartz overgrowth, and carbonate cement. It is important to note that mechanical and chemical sedimentation are not mutually exclusive and may occur simultaneously.

5.4. Color Heterogeneity and Implications

Unlike the pedogenesis of laterite, numerous studies have demonstrated that the red hue of continental red beds, which develops during diagenesis, may not necessarily be indicative of climate [15,33,50]. From the Great Oxygenation Event to the Miocene epoch, many continental red beds have been known to form across a range of geological periods and tectonic settings [8,16,51]. The diagenetic process of reddening in continental red beds is mostly influenced by factors such as the sediment sources, redox conditions, and the duration and depth of burial. In the case of the Danxia Formation, deposition began in the Late Cretaceous period and was subsequently uplifted during the Paleogene period due to tectonic activity, in that series of units within the formation experienced similar burial times and depths. Interestingly, however, during the deposition of the Danxia Formation, South China experienced a brief arid period [28], which caused the sedimentary environment of the Danxia Basin to shift from an alluvial fan to an ancient desert and back again. These two sedimentary facies differed not only in climate but also in the composition, roundness, and sorting of clastic sediments. The latter may result in the vertical color heterogeneity within the red beds. In the alluvial fan facies, clastic particles were poorly sorted and had low roundness. They contained more iron-bearing minerals, providing sufficient authigenic iron sources. In contrast, the ancient desert facies had good mineralogical maturity with fewer iron-bearing mineral fragments. As a result, after diagenetic alteration, the alluvial fan facies have abundant fine hematite, mainly reddish-purple to maroon. The ancient desert facies have fewer hematite, resulting in a reddish-brown color. Whole-rock geochemical analyses support this view, showing higher total iron content in reddish-purple and maroon red beds compared to reddish-brown red beds. Although both the ancient desert and alluvial fan facies underwent diagenesis and turned red, differences in sediment sources caused color fluctuations in each member. Similar color heterogeneity observed in other continental red beds may have the same causes. While the color of continental red beds does not indicate climate, changes in the sedimentary environment can affect the sediment sources which result in color variation.

6. Conclusions

During the early deposition period, the sediments displayed hues of yellow or light red due to the presence of iron oxyhydroxides such as goethite. However, it was during diagenesis that the formation underwent a transformation and reddened. This change in color can be attributed to fine-grained hematites, which are the alteration products of iron-bearing clastic particles (biotite, ilmenite, magnetite, etc.) from surrounding areas into the Danxia basin. These fine-grained hematites mixed with clay minerals and formed a red coating on the surface of detrital grains or were distributed in the matrix and fractures as dissemination and clusters. The color of members within the Danxia Formation varies from reddish-brown to reddish-purple due to changes in the relative content and particle size of hematite and goethite. And these variations are primarily controlled by sediment sources.

Supplementary Materials: The following supporting information can be downloaded at: <https://www.mdpi.com/article/10.3390/min13081054/s1>. Figure S1. EPMA results of FeO* and SiO₂ varies with the concentration of red pigment; Figure S2. SEM images of iron oxides in cracks; Figure S3. EDX mapping image of the edges of detrital quartz; Table S1. Trace elements compositions from bulk samples of fluctuant colors; Table S2. Rare earth elements (REE) compositions from bulk samples of fluctuant colors.

Author Contributions: Conceptualization, W.H. and Z.Y.; methodology, W.H.; investigation, W.H. and J.H.; resources, K.Z. and H.L.; data curation, W.H.; writing—original draft preparation, W.H.; writing—review and editing, W.H. and Z.Y.; visualization, J.H.; supervision, Z.Y.; project administration, Z.Y.; funding acquisition, Z.Y. All authors have read and agreed to the published version of the manuscript.

Funding: This research was funded by the Guangdong provincial Natural Science Foundation (Grant 2021S1515011472) and the Guangdong Special Fund for National Park Construction (Grant 2021GJGY026).

Data Availability Statement: The data associated with this paper are confidential and may be available by contacting the authors.

Acknowledgments: We thank Xiaoning Chen and Ruimei Xu (Instrumental Analysis and Research Center, Sun Yat-Sen University) for their SEM assistance, Catherine Chagué (The University of New South Wales) for her suggestions, and Wen Li and Chaofang Dai (School of Earth Science and Engineering, Sun Yat-sen University) for providing the necessary facilities.

Conflicts of Interest: The authors declare no conflict of interest.

References

1. Li, Q. Research on Danxia landform by geographers of Sun Yat-sen University. *J. Sun Yat-Sen Univ.* **2011**, *51*, 71–78. (In Chinese)
2. Peng, H.; Pan, Z.; Yan, L.; Scott, S. A review of the research on red beds and Danxia landform. *Acta Geogr. Sin.* **2013**, *68*, 1170–1181. (In Chinese) [[CrossRef](#)]
3. Pan, Z.; Ren, F.; Peng, H. Development of red bed landform in the western United States and a comparison with Danxia landform in southeast China. *Geogr. Res.* **2018**, *37*, 2399–2410. (In Chinese)
4. Guo, F.; Chen, L.; Yan, Z.; Liu, F.; Pan, Z.; Zhang, W.; Hu, H. Definition, classification, and danxianization of Danxia landscapes. *Acta Geol. Sin.* **2020**, *94*, 361–374. (In Chinese) [[CrossRef](#)]
5. Migoñ, P. Geomorphology of conglomerate terrains Global overview. *Earth-Sci. Rev.* **2020**, *208*, 103302. [[CrossRef](#)]
6. Hill. UNESCO World Heritage Evaluation Process and U.S.A. Sites. In *The First International Symposium on Danxia Landform; Administrative Committee of Mt. Danxiashan Global Geopark: Shaoguan, China, 2009*; pp. 302–308.
7. United Nations Educational, S.A.C.O. China Danxia. Available online: <https://whc.unesco.org/en/list/1335> (accessed on 13 April 2023).
8. He, W.; Yang, Z.; Du, H.; Hu, J.; Zhang, K.; Hou, W.; Li, H. Micro-Mechanisms and Implications of Continental Red Beds. *Minerals* **2022**, *12*, 934. [[CrossRef](#)]
9. Folk, R.L. Reddening of desert sands: Simpson Desert, N.T., Australia. *J. Sediment. Petrol.* **1976**, *46*, 604–615. [[CrossRef](#)]
10. Krynine, P.D. The origin of red beds. *Trans. N. Y. Acad. Sci.* **1949**, *11*, 60–68. [[CrossRef](#)]
11. Krynine, P.D. *Petrology, Stratigraphy, and Origin of the Triassic Sedimentary Rocks of Connecticut*; State Geological and Natural History Survey: Berkeley, CA, USA, 1950; p. 247.
12. Van Houten, F.B. Climatic significance of red beds. *Descr. Paleoclimatol.* **1961**, *21*, 89–139.
13. Van Houten, F.B. Origin of Red Beds—Some Unsolved Problems. In *Problems in Palaeoclimatology, Proceedings of the NATO Paleoclimate Conference, Newcastle upon Tyne, UK, 7–12 January 1963*; Inter-Science Pub. Inc.: New York, NY, USA, 1964; pp. 647–660.
14. Walker, T.R. Formation of red beds in moist tropical climates: A hypothesis. *Geol. Soc. Am. Bull.* **1974**, *85*, 633–638. [[CrossRef](#)]
15. Walker, T.R. Diagenetic origin of continental red beds. In *The Continental Permian in Central, West, and South Europe*; Springer: Berlin/Heidelberg, Germany, 1976; pp. 240–282.
16. Turner, P. *Continental Red Beds*; Elsevier Scientific Publishing Company: Amsterdam, The Netherlands, 1980.
17. Bankole, O.M.; El Albani, A.; Meunier, A.; Rouxel, O.J.; Gauthier-Lafaye, F.; Bekker, A. Origin of red beds in the Paleoproterozoic Franceville Basin, Gabon, and implications for sandstone-hosted uranium mineralization. *Am. J. Sci.* **2016**, *316*, 839–872. [[CrossRef](#)]
18. Xiao, Y.; Li, Y.; Ding, H.; Li, Y.; Lu, A. The Fine Characterization and Potential Photocatalytic Effect of Semiconducting Metal Minerals in Danxia Landforms. *Minerals* **2018**, *8*, 554. [[CrossRef](#)]
19. Fu, W.; Turner, P.; Clements, T.; Spencer, A.R.T.; Yu, J.; Yang, Y.; Guo, B.; Ning, Z.; Zhuo, X.; Riley, M.S.; et al. Taphonomic and diagenetic implications of reduction spot formation in Cretaceous red beds from the Jiaolai Basin, Eastern China. *J. Asian Earth Sci.* **2023**, *243*, 105533. [[CrossRef](#)]
20. Bensing, J.P.; Mozley, P.S.; Dunbar, N.W. Importance of Clay in Iron Transport and Sediment Reddening: Evidence from Reduction Features of the Abo Formation, New Mexico, U.S.A. *J. Sediment. Res.* **2005**, *75*, 562–571. [[CrossRef](#)]
21. Stel, H. Diagenetic crystallization and oxidation of siderite in red bed (Buntsandstein) sediments from the Central Iberian Chain, Spain. *Sediment. Geol.* **2009**, *213*, 89–96. [[CrossRef](#)]
22. Eren, M.; Kadir, S.; Kapur, S.; Huggett, J.; Zucca, C. Colour origin of Tortonian red mudstones within the Mersin area, southern Turkey. *Sediment. Geol.* **2015**, *318*, 10–19. [[CrossRef](#)]
23. Aehnelt, M.; Hilse, U.; Pudlo, D.; Heide, K.; Gaupp, R. On the origin of bleaching phenomena in red bed sediments of Triassic Buntsandstein deposits in Central Germany. *Geochem. -Ger.* **2021**, *81*, 125736. [[CrossRef](#)]
24. Zhang, X. Division and Correlation of Cretaceous in Danxia Basin. *J. Stratigr.* **1992**, *16*, 81–95. (In Chinese)
25. Zhu, C.; Wu, L.; Zhu, T.; Hou, R.; Hu, Z.; Tan, Y.; Sun, W.; Jia, T.; Peng, H. Experimental studies on the Danxia landscape morphogenesis in Mt. Danxiashan, South China. *J. Geogr. Sci.* **2015**, *25*, 943–966. [[CrossRef](#)]

26. Chen, L.; Li, X.; Guo, F.; Li, P.; Li, Y.; Liu, X. Characteristics and Origin of Honeycombs in the Danxiashan Global Geopark in South China. *Geol. Rev.* **2018**, *64*, 895–904. (In Chinese) [[CrossRef](#)]
27. Huang, Q. Geological Tectonic Setting and Zoning of Danxia Landform in Guangdong Province. *Trop. Geogr.* **2016**, *36*, 935–943. (In Chinese) [[CrossRef](#)]
28. Liu, J. Research on Formation Mechanism and Geo-Scientific Effects of Danxia Landform in Southeast China. Ph.D. Thesis, Central South University, Changsha, China, 2009.
29. Liu, F. Sedimentary Environment and Geomorphologic Evolution of Danxia Landscape Layer from Danxiashan, Guangdong Province. Ph.D. Thesis, Chengdu University of Technology, Chengdu, China, 2020.
30. Zhan, Y. Study on Sedimentary Environments of the Late Cretaceous Danxia Formation in Mt. Danxiashan of Northern Guangdong. Master's Thesis, East China Institute of Technology, Nanchang, China, 2021.
31. Rasmussen, B.; Muhling, J.R. Syn-tectonic hematite growth in Paleoproterozoic Stirling Range “red beds”, Albany-Fraser Orogen, Australia: Evidence for oxidation during late-stage orogenic uplift. *Precambrian Res.* **2019**, *321*, 54–63. [[CrossRef](#)]
32. Yan, M.; Chi, Q. *The Chemical Compositions of the Continental Crust and Rocks in the Eastern Part of China*; Science Press: Beijing, China, 2005; p. 171.
33. Walker, T.R.; Larson, E.E.; Hoblitt, R.P. Nature and origin of hematite in the Moenkopi Formation (Triassic), Colorado Plateau; a contribution to the origin of magnetism in red beds. *J. Geophys. Res.* **1981**, *86*, 317–333. [[CrossRef](#)]
34. Grygar, T.; Dědeček, J.; Kruiver, P.P.; Dekkers, M.J.; Bezdička, P.; Schneeweiss, O. Iron oxide mineralogy in late Miocene red beds from La Gloria, Spain: Rock-magnetic, voltammetric and Vis spectroscopy analyses. *Catena* **2003**, *53*, 115–132. [[CrossRef](#)]
35. McBride, E.F. Significance of color in red, green, purple, olive, brown, and gray beds of Difunta Group, northeastern Mexico. *J. Sediment. Petrol.* **1974**, *44*, 760–773. [[CrossRef](#)]
36. Scheinost, A.C.; Schwertmann, U. Color identification of iron oxides and hydroxysulfates: Use and limitations. *Soil. Sci. Soc. Am. J.* **1999**, *63*, 1463–1471. [[CrossRef](#)]
37. Cornell, R.M.; Schwertmann, U. *The Iron Oxides: Structure, Properties, Reactions, Occurrences, and Uses*; Wiley-vch Weinheim: Weinheim, Germany, 2003; Volume 2.
38. Jiang, Z.; Liu, Q.; Roberts, A.P.; Dekkers, M.J.; Barrón, V.; Torrent, J.; Li, S. The Magnetic and Color Reflectance Properties of Hematite: From Earth to Mars. *Rev. Geophys.* **2022**, *60*, e2020RG000698. [[CrossRef](#)]
39. Pan, F.; Guo, Z.; Liu, H.; Wang, B.; Li, Z.; Zhuang, Z. High-Resolution Distribution and Biogeochemical Behavior of Phosphorus and Iron at Sediment-Water Interface of Tidal Flat. *Earth Sci.* **2018**, *43*, 4109–4119. (In Chinese)
40. Huang, T.; Wang, R.; Shen, B. The phosphorus cycle and biological pump in Earth's middle age: Reappraisal of the “Boring Billion”. *Chin. Sci. Bull.* **2022**, *67*, 1614–1623. (In Chinese) [[CrossRef](#)]
41. Reich, M.; Simon, A.C.; Barra, F.; Palma, G.; Hou, T.; Bilinker, L.D. Formation of iron oxide–apatite deposits. *Nat. Rev. Earth Environ.* **2022**, *3*, 758–775. [[CrossRef](#)]
42. Turner, P.; Archer, R. The role of biotite in the diagenesis of red beds from the Devonian of northern Scotland. *Sediment. Geol.* **1977**, *19*, 241–251. [[CrossRef](#)]
43. Villa, I.M.; Bosio, G. “Excess Ar” by laboratory alteration of biotite. *Geology* **2022**, *51*, 121–125. [[CrossRef](#)]
44. Wu, Z.; Peng, H. A Study on the Formation and Development Rules of the Red Beds in Guangdong Province. *Trop. Geogr.* **2005**, *26*, 301–306. (In Chinese)
45. Qi, D.; Yu, R.; Zhang, R.; Ge, Y.; Li, J. On the Spatial Pattern of Danxia Landform in China. *Acta Geogr. Sin.* **2005**, *60*, 41–52. (In Chinese)
46. Pan, Z.; Peng, H. Comparative Study on the Global Distribution and Geomorphic Development of Red Beds. *Sci. Geogr. Sin.* **2015**, *35*, 1575–1584. (In Chinese)
47. Yan, L.; Peng, H.; Zhang, S.; Zhang, R.; Kašanin-Grubin, M.; Lin, K.; Tu, X. The Spatial Patterns of Red Beds and Danxia Landforms: Implication for the formation factors—China. *Sci. Rep.-UK* **2019**, *9*, 1961. [[CrossRef](#)]
48. Zhou, C.; Yang, X.; Liang, Y.; Du, Z.; Liu, Z.; Huang, W.; Ming, W. Classification of Red-Bed Rock Mass Structures and Slope Failure Modes in South China. *Geosciences* **2019**, *9*, 273. [[CrossRef](#)]
49. Blodgett, R.H.; Crabaugh, J.P.; McBride, E.F. The color of red beds—A geologic perspective. *Soil. Color.* **1993**, *31*, 127–159.
50. Sheldon, N.D. Do red beds indicate paleoclimatic conditions? A Permian case study. *Palaeogeogr. Palaeoclimatol. Palaeoecol.* **2005**, *228*, 305–319. [[CrossRef](#)]
51. Kuang, H.; Bai, H.; Peng, N.; Qi, K.; Wang, Y.; Chen, X.; Liu, Y. Temporal and spatial distribution of Precambrian red beds and their formation mechanisms. *Geosyst. Geoenviron.* **2022**, *1*, 100098. [[CrossRef](#)]

Disclaimer/Publisher's Note: The statements, opinions and data contained in all publications are solely those of the individual author(s) and contributor(s) and not of MDPI and/or the editor(s). MDPI and/or the editor(s) disclaim responsibility for any injury to people or property resulting from any ideas, methods, instructions or products referred to in the content.